minerals

MDPI

Review

Engineered Artificial Minerals (EnAMs): Concept, Design Strategies, and Case Studies

Wensheng Han [1], Joao Weiss [2], Xiang Lu [1], Daniel Munchen [2], Chuling Jiang [1], Hugo Lucas [2], Mengjie Ran [1,3], Wen Chen [1,*] and Bernd Friedrich [2,*]

[1] Changsha Research Institute of Mining and Metallurgy Co., Ltd., Changsha 410012, China; hanws0@minmetals.com (W.H.); xianglu@minmetals.com (X.L.); jiangcl@minmetals.com (C.J.); 225601022@csu.edu.cn (M.R.)
[2] IME Process Metallurgy and Metal Recycling, RWTH Aachen University, Intzestraße 3, 52056 Aachen, Germany; jweiss@metallurgie.rwth-aachen.de (J.W.); dmunchen@metallurgie.rwth-aachen.de (D.M.); hlucas@metallurgie.rwth-aachen.de (H.L.)
[3] School of Minerals Processing and Bioengineering, Central South University, Changsha 410083, China
* Correspondence: wenchen@minmetals.com (W.C.); bfriedrich@metallurgie.rwth-aachen.de (B.F.)

Abstract

With the continuous development of easily accessible resources, the exploitation of complex mineral resources, metallurgical waste slag containing high-value metals, and secondary resources is gradually becoming a mainstream trend. Due to the complex distribution characteristics of elements in these resources, efficient recycling is difficult to achieve. A phase reconstruction strategy has been proposed to address the distribution forms of elements. The phase reconstruction strategy employs pyrometallurgical methods to subject complex resources to high-temperature smelting and cooling crystallization. In the cooling crystallization process, the target elements in melt are selectively enriched into engineered artificial minerals (EnAMs). Then, the target elements can be recovered by subsequently separating these EnAMs. However, the concept of and design strategies for EnAMs are still unclear. In this review, the concept of EnAMs is proposed based on previous studies. This review explores how to design EnAMs by phase equilibrium studies and utilizing geochemical behaviors. Additionally, the application cases of EnAMs in treating challenging tantalum–niobium and rare earth element (REE) resources, secondary resource recycling, and metallurgical slag were collected. Furthermore, the challenges and future perspectives of EnAMs for complex resources are discussed.

Keywords: engineered artificial minerals; phase reconstruction; selective enrichment; recovery

Academic Editor: Sunil Kumar Tripathy

Received: 22 September 2025
Revised: 17 October 2025
Accepted: 24 October 2025
Published: 29 October 2025

Citation: Han, W.; Weiss, J.; Lu, X.; Munchen, D.; Jiang, C.; Lucas, H.; Ran, M.; Chen, W.; Friedrich, B. Engineered Artificial Minerals (EnAMs): Concept, Design Strategies, and Case Studies. *Minerals* **2025**, *15*, 1129. https://doi.org/10.3390/min15111129

1. Introduction

Mineral resources are the necessary material foundation for humanity's advancement towards modernization, automation, and intelligence. Most cutting-edge technologies, such as the batteries of electric vehicles, the high-temperature alloys used in the aerospace field, the semiconductor materials used in 5G communication, and the rare earth permanent magnets used for artificial intelligence robots, rely on the stable supply of key metal resources. The occurrence of mineral resources not only determines the path and speed of technological development but also profoundly affects the layout of global industrial chains and resource competition. According to statistics, over 50% of lithium carbonate

resources in China are used for lithium battery production [1], and 56% of platinum-group metals (PGMs) in the world are used in automotive catalysts [2]. However, with the increasing depletion of high-grade primary mineral resources and the acceleration of global industrialization, resource shortages and environmental pollution problems are becoming increasingly prominent. The traditional linear economic model of "resource consumption–product manufacturing–pollution emission" is increasingly struggling to sustain the needs of sustainable development. Resource development is gradually shifting to handle complex mineral resources, metallurgical waste slag rich in high-value metals, and secondary resources in urban mines. The comprehensive utilization of these three types of resources has become a breakthrough important to solving resource constraints and achieving a circular economy.

Complex mineral resources, especially rare and precious metal resources, are characterized by low grades, fine particle sizes, and symbiosis with other elements. Many resources have huge reserves, but they cannot be developed and utilized due to the limitations of resource development technologies. Taking niobium resources as an example, the current niobium resource output from Brazil and Canada accounts for more than 90% of the world's total [3]. Actually, there are many large niobium deposits outside of Brazil and Canada [4], such as the Bonga deposit in Angola (824 Mt, 0.48% Nb_2O_5), the Mabounie deposit in Gabon (401.2 Mt at 1.11% Nb_2O_5), the Ghurayyah deposit in Saudi Arabia, and Bayan Obo in China (2.2 Mt at 0.13% Nb_2O_5) [5].

In the field of secondary resource recycling, the circular economy concept centered on secondary resource regeneration has become a global consensus. Valuable elements in the secondary resource can be recovered, such as in the recovery of precious metals (gold, silver, rare earth elements, and copper), as well as harmful substances like lead and mercury, from electronic waste (e.g., discarded appliances or printed circuit boards) [6–8]; lithium from spent lithium-ion batteries [9,10]; and platinum from spent catalysts [11]. The concentration of platinum-group metals (PGMs), lithium, and cobalt in urban mines (such as electronic waste, spent catalysts, and spent lithium-ion batteries) is significantly higher than that in primary ores [12–14]. For instance, mass-produced computer motherboards contain approximately 200–250 $g \cdot t^{-1}$ of gold and about 80 $g \cdot t^{-1}$ of palladium, while mobile phones can contain up to 350 $g \cdot t^{-1}$ of gold and 130 $g \cdot t^{-1}$ of palladium [15]. The content in used ceramic catalytic converters and spent metal catalysts has reached 2596 $g \cdot t^{-1}$ and 7874 $g \cdot t^{-1}$, respectively [16]. This is clearly much higher than the gold or PGM content in primary ores (averaging < 10 $g \cdot t^{-1}$) [12]. Aside from PGMs, the content of rare metals in rechargeable batteries and hybrid/electric vehicle (HEV) batteries overs 180 $g \cdot kg^{-1}$ [17–19]. Permanent NdFeB magnets in hard disks, microphones, and speakers contain neodymium (Nd, 190–350 $g \cdot kg^{-1}$) and dysprosium (Dy, 14–45 $g \cdot kg^{-1}$) [19,20]. Therefore, an economic advantage arises from the higher concentrations of valuable metals in electronic and electrical waste compared to ores. E-waste recycling offers a way to recover rare earth metals and other critical raw materials, reducing primary production [21–23]. With the advancement of new energy technologies, it is expected that by 2030 the market for rechargeable batteries in electric vehicles will exceed 7000 GWh, while the overall battery market will surpass 10,000 GWh [24], resulting in even more secondary resources. In 2019, approximately 53.6 million tons of e-waste were generated worldwide, and it is estimated that this amount will increase to around 74 million tons by 2030. If current trends continue, the amount could even rise to 120 million tonnes by 2050. In Germany, the amount of electrical and electronic equipment waste (WEEE) was 12.5 kg per capita, slightly above the EU average (10.5 kg per capita). This large volume of e-waste to be processed and the complex recycling processes need the further development of e-waste recycling and integration across the technical, economic, social, and environmental spheres [25,26].

In addition to complex mineral resources, metal resources in considerable amounts are contained in metallurgical waste slag. The term metallurgical waste slag refers to solid waste generated during pyrometallurgical processes, such as steel slag, blast furnace slag, and copper slag; e.g., fayalitic slags, which contain valuable elements such as scandium (Sc), titanium (Ti), nickel (Ni), copper (Cu), and iron (Fe), as well as harmful elements such as chromium (Cr) and lead (Pb) [27]. Originated from the smelting of electronic scrap incorporated into copper production, fayalitic slag is mainly formed by SiO_2 and FeO, but often contains CaO and other oxides, which consequently implies a high oxygen content. Since most valuable metals are present in diluted concentrations and show high oxygen affinity, the consequent loss of metallurgical waste is inevitable. According to statistics, smelteries globally produce approximately 190–290 million tons of steel slag and 70 million tons of copper slag annually [28]. However, the recovery rate of metals in global metallurgical waste slag is low, and the problems of resource waste and environmental pollution coexist.

To address the challenges of reusing complex mineral resources and metallurgical waste rich in high-value metals, as well as secondary resources in urban mines, the recrystallization strategy is employed to change the distribution forms of elements, as shown in Figure 1. After a rough concentration process, target elements in these resources are induced to a directional and selective enrichment in melts, resulting in what are known as engineered artificial minerals (EnAMs). Then, the target elements can be recovered by subsequently separating these EnAMs. This strategy provides a solution for the beneficiation and recycling of complex resources. In this review, the concepts, design methods, and application cases of EnAMs are summarized. The challenges of and future perspectives related to EnAMs are also proposed at the end of the manuscript.

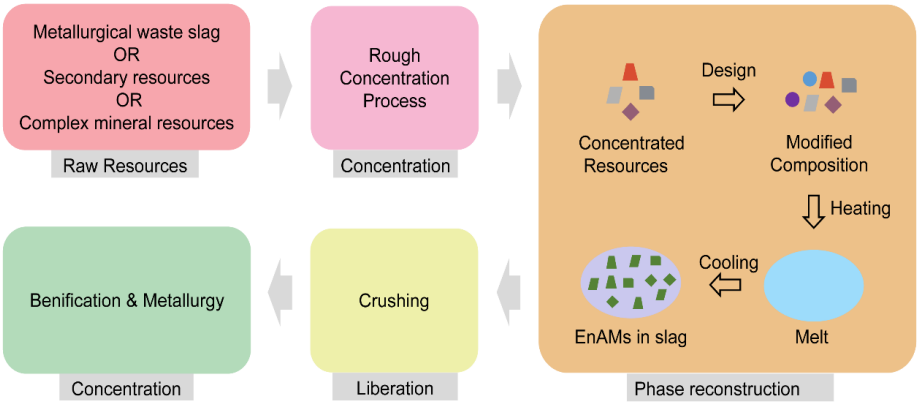

Figure 1. Application of engineered artificial minerals (EnAMs) in the recovery route of resources.

2. Concept of EnAMs

Engineered artificial minerals (EnAMs) are synthetic mineral phases with a high element concentration in slag created through high-temperature melting–cooling crystallization or phase transformation processes, which disrupt the original elemental distribution states [29–31]. By artificially designing and controlling the chemical composition of metallurgical slags, EnAMs enable the targeted centralized enrichment of specific elements. During the high-temperature melting stage in the heating process, chemical bonds within the raw materials are broken, resulting in a disordered atomic arrangement. The subsequent crystallization stage during the cooling process provides opportunities for atomic reorganization. Through the precise regulation of slag composition, tailored physicochemical environments are established to guide the selective combination of target elements, ultimately forming highly concentrated mineral phases. EnAMs mimic natural mineral

formation processes, sharing similarities with the cooling and solidification of magmatic melts, including elemental partitioning between phases, migration dynamics, dissolution–precipitation behaviors, and component volatilization. However, critical differences exist between artificial and natural mineralization, particularly in terms of pressure conditions (e.g., atmospheric vs. crustal hyperpressure environments) and formation timescales (days vs. geological epochs). Hence, the design and synthesis of EnAMs require interdisciplinary collaboration across metallurgical engineering, chemistry, ore-forming geochemistry, and mineralogy to optimize phase engineering under controlled industrial conditions.

3. Design of EnAMs

Because the formation mechanisms of engineered artificial minerals (EnAMs) share similarities and differences with those of natural minerals, the design of EnAMs can be achieved by phase equilibria studies and simulating ore-forming geochemical environments, as shown in Figure 2. When the simulated physicochemical ore-forming environment satisfies the conditions for mineral formation, the designed artificial minerals may exhibit phase consistency or crystal structure consistency with natural minerals. When the composition and properties of the raw materials differ from those during elemental mineralization, new phases can be formed as carriers for element enrichment. Therefore, the design of EnAMs primarily involves considering phase equilibrium relationships and simulating ore-forming geochemical environments.

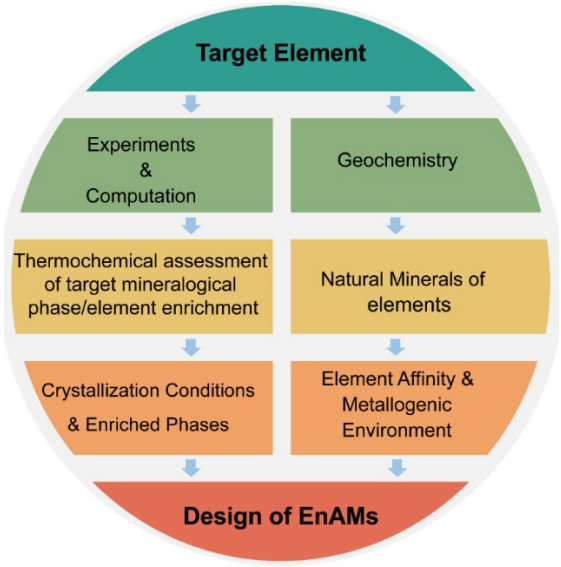

Figure 2. Design strategies for targeted element enrichment in engineered artificial minerals (EnAMs).

3.1. Phase Equilibrium Study

Phase equilibrium is an important theory for studying the equilibrium state of matter in multiphase systems [32,33]. In the design of EnAMs, phase equilibrium studies play a decisive role in understanding the phases formed by key elements during the cooling crystallization process. Phase diagrams based on the phase equilibrium provide a visual understanding of the types and quantities of phases that may exist in a system, as well as their interconversion relationships, under different temperature, pressure, and composition conditions [34]. Phase diagrams can be obtained from thermodynamic calculation and experimental analysis. Phase stability and phase diagram predictions are primarily conducted using thermodynamic software such as FactSage, Pandat, and the OpenCalphad (OCA) package. The experimental analysis mainly includes characterizing phases and their

composition in different conditions through characterization tools, including X-ray powder diffraction and electron probe microanalysis.

According to the compositions of resources, a phase diagram can be obtained through experiments and calculations. The corresponding formation conditions of enriched phases, such as the composition and temperature range, are also determined in the phase diagram. Taking a common ternary system A-B-C phase diagram as an example, by analyzing the various phase regions within the diagram, it is possible to determine that the target phase can be formed when the three components A, B, and C are within a specific compositional range and the temperature is controlled within a certain interval. In studies on the recovery and utilization of smelting slag containing titanium resources, high-temperature melting–cooling crystallization is employed to transform titanium-containing phases. Phase equilibrium studies based on the CaO-SiO_2-TiO_2 system can determine that titanium is mainly enriched in perovskite, as shown in Figure 3 [35]. Perovskite should be chosen as a targeted EnAM for recycling titanium. By further adding the components of the phase diagram, the changing trends in the perovskite crystallization region and crystallization temperature can be obtained in complex multi-component systems containing MgO [36–38], Al_2O_3 [39], and Cr_2O_3 [35]. In multi-component systems, the interaction between different elements can affect the crystal structure and chemical composition of the phases. For example, adding 5 wt% Cr_2O_3 to the CaO-SiO_2-TiO_2 ternary phase diagram proves that the addition of Cr_2O_3 promotes the crystallization of perovskite by extending the primary phase region of perovskite to a higher SiO_2 region, thereby facilitating the recovery of Ti [35]. Additionally, the influence of oxygen partial pressure on crystallization can also be determined by a CaO-SiO_2-Ti_xO_y phase diagram [40–42]. In the study of crystallization behaviors of lithium-bearing slag, the existence of manganese (Mn) affects the phases of lithium-bearing EnAMs [43]. The presence of manganese and its valence changes will form Li-Mn-Al spinel solid solutions or lithium manganates [44]. By adding MgO and Al_2O_3, hausmannite is effectively suppressed and a solid solution between the spinels of $Mn^{2+}Mn^{3+}{}_2O_4$, $MgAl_2O_4$ and $Mn^{2+}Al_2O_4$ is formed [45]. The calculated equilibrium solidification process of the Li_2O-Al_2O_3-SiO_2-CaO-MnO system proves that γ-lithium aluminate as primarily crystalline was precipitated as the temperature decreased [46]. When the temperature decreases to around 1350 °C, only γ-lithium aluminate forms a liquid. Hence, controlling the crystallization temperature can effectively control the crystalline phases.

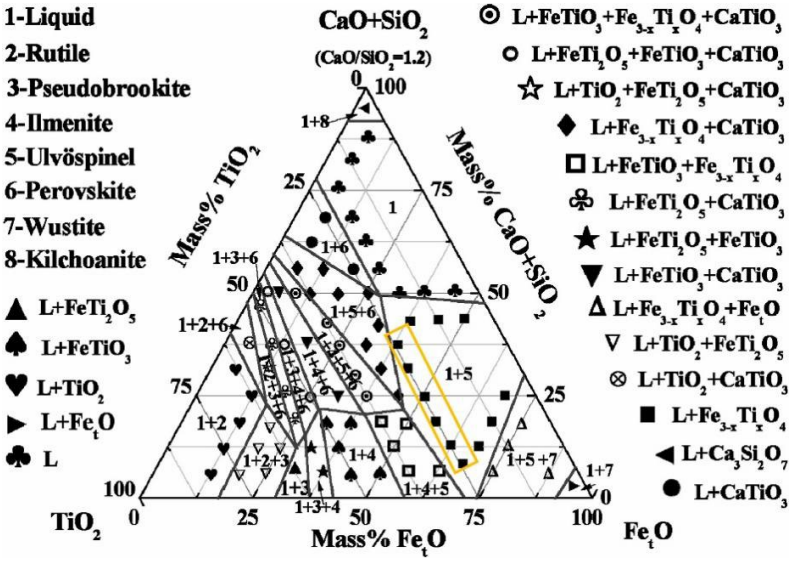

Figure 3. Phase equilibrium diagram for the Fe_tO-TiO^2-CaO-SiO_2 at 1673 K (Reproduced with permission from [47], published by Elsevier Ltd., 2024).

In addition to being based on resource composition, phase diagrams can also be designed based on the composition of anticipated EnAMs. The designed phase diagrams are used to study phase equilibrium relationships and determine crystallization conditions. Then, in the actual batching process, the corresponding raw materials can be accurately weighed according to this compositional range to ensure that the subsequent crystallization process proceeds in the direction of forming the target phase. For example, if titanium-containing resources are to be converted into ilmenite ($TiFeO_3$) minerals or pseudobrookite, the phase equilibrium relationship can be studied by designing a multi-component system phase diagram containing iron (Fe^{2+} or Fe^{3+}) [47,48]. As shown in Figure 3, the designed phase diagram determines the crystallization interval for the formation of $TiFeO_3$ and the corresponding relative content of each component. Additionally, when constructing apatite ($Ca_5(PO_4)_3(F,Cl,OH)$) as target EnAMs in a targeting slag containing rare earth elements (REEs), the precipitation region of apatite can be determined through phase equilibrium studies of multi-component systems containing phosphorus, calcium, and rare earths [49].

Phase diagrams also can guide the cooling process [50]. The cooling process is a critical step in the formation of EnAMs, and phase diagrams provide important guidance for controlling the cooling process. Different cooling rates and cooling paths lead to different degrees of atomic diffusion and rearrangement, which in turn affects the final formed phases [51,52]. For example, the long-term storage of stainless-steel slag containing a large amount of chromium can cause hexavalent chromium to pollute the environment. Therefore, designing EnAMs enriched in chromium can promote the green manufacturing practice of the metallurgical industry. When chromium slag reaches phase equilibrium in the range of 800–1600 °C, chromium is mainly enriched in the amorphous phase, diopside and akermanite, and spinel [53]. Based on a comprehensive judgment of the enrichment rate of chromium in EnAMs and the economy of crystallization temperature, it is considered that 800 °C is conducive to the maximum stabilization of Cr in the spinel phase [53]. Therefore, the slag/melt can be quickly cooled down to 800 °C to allow the spinel phase to preferentially precipitate, avoiding chromium in diopside and akermanite. A reasonable cooling regime can be formulated based on the crystallization temperature range and transformation temperature of each phase in the phase diagram. The accurate control of the cooling process based on the phase diagram can realize the effective adjustment of EnAMs.

3.2. Utilizing Geochemical Behaviors

In the formation of natural minerals, the distribution of most rare metals is relatively concentrated. For example, pyrochlore is the main carrier mineral for niobium. The carrier minerals of niobium in the Brazilian Catalão and Araxá mines, and the Canadian Niobec niobium mine are pyrochlore [54]. Gallium resources are mainly concentrated in bauxite deposits [55,56]. Therefore, the design of EnAMs for rare elements can refer to the ore-forming characteristics of elements. Based on the ore-forming environment of minerals, such as temperature, pressure, composition, and redox environment [57], a simulated geochemical formation environment should be constructed. This method is limited in its application due to economic constraints. In addition, simulating the geochemical process environment of ore formation is difficult to construct. However, in the design process of artificial minerals, the ore-forming principle of geochemical and the physical-chemical environment can still provide support in terms of design direction. Simultaneously, when artificial minerals are consistent with that of natural minerals, the existing beneficiation, sorting, and separation technologies are mature, leading to high applicability.

1. Simulating Element Affinity

According to Goldschmidt's classification of elements based on their geochemical behavior during ore formation and preferred host phases, elements are broadly divided based

on their affinity into lithophile, siderophile, chalcophile and atmophile elements [58–60]. Based on the geochemical affinity of the element, lithophile, siderophile, and chalcophile elements preferentially enter silicate melts, metallic (iron) phases, or sulfides, respectively, during phase partitioning. Lithophile elements (Li, Na, K, Mg, Ca, Al, Si, etc.) tend to combine with oxygen and are enriched in the silicates of the earth's crust and mantle. Siderophile elements (Fe, Ni, Co, Mn, Mo, W, Au, etc.) readily combine with metallic iron and are enriched in the earth's core. Chalcophile elements (Cu, Zn, As, Se, Pb, S, Ag, Cd, In, Sn, Sb, Te, Hg, Bi, Tl, etc.) tend to combine with sulfur, forming sulfide minerals. The affinity of Ru, Rh, Pd, Re, Os, Ir, and Pt can be either chalcophile or siderophile, depending on the ore-forming environment. The element affinity in the actual pyrometallurgy is similar with geochemistry, as shown in Figure 4 [61]. lithophile elements correspond to metallurgical slag, such as blast furnace slag, converter slag, refining slag, etc. These slags often include more than two kinds of Al_2O_3, SiO_2, FeO, MgO, CaO. The chalcophile elements correspond to matte in the metallurgical process, usually copper matte or nickel/cobalt matte (such as Cu_2S, Ni_3S_2, CoS). siderophile correspond to ferrophiles or alloys. The atmophile elements correspond to the gas phase in the metallurgical process.

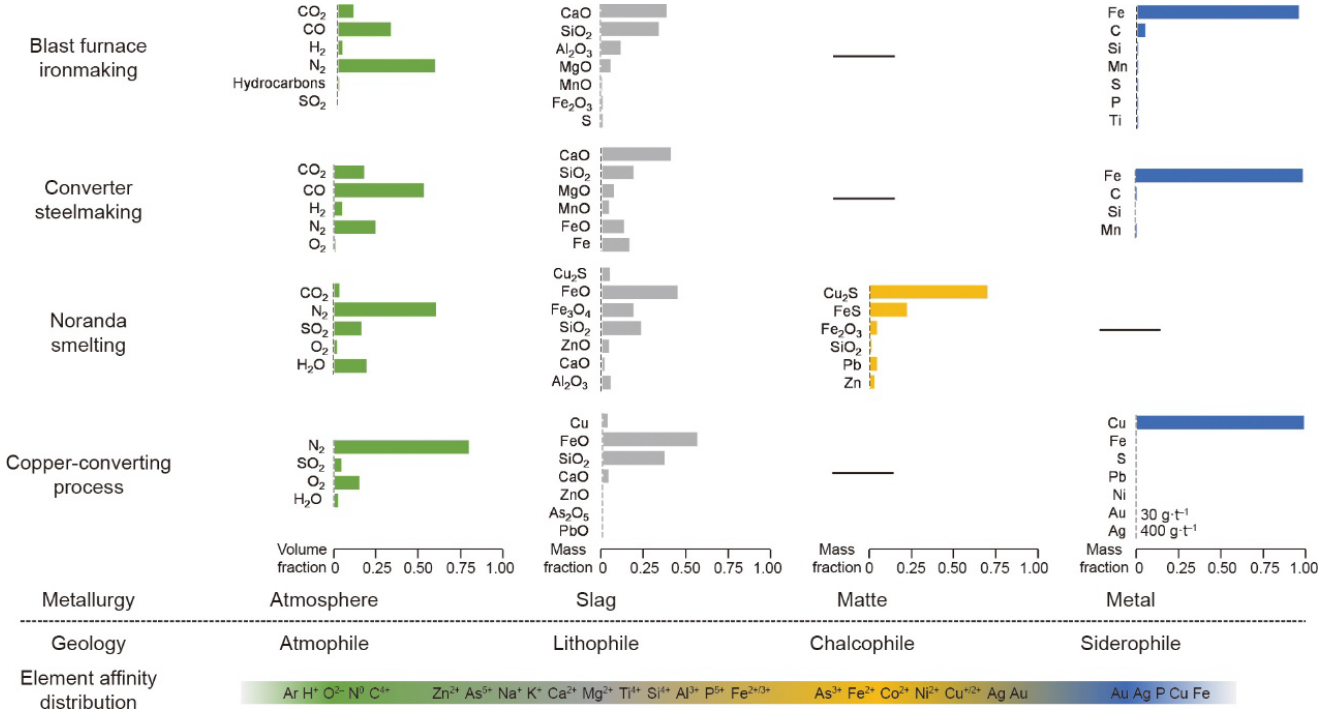

Figure 4. Similar elements affinity in geochemistry and pyrometallurgy [61].

Based on the Goldschmidt classification, the path for designing target minerals has a general direction. When designing chalcophile elements, EnAMs can be designed as metal sulfides formed in low-oxygen content environments. The transformation and recovery of metals can be achieved. For example, lead, arsenic, silver, gold, platinum, and copper transform into metal sulfides as matte, which can be separated from slag [62–64]. When treating copper smelting slag under pressurized oxygen atmosphere and low acidity conditions, iron and silicon in the slag transforms and reconstructs into hematite and amorphous silica, respectively [65]. Regarding iron-containing slag, the iron in the slag can form EnAMs in the form of oxides under oxygen-rich conditions, such as hematite (Fe_2O_3) [66] or $(Mn,Mg)_xFe_{3-x}O_4$ [67]. Under reducing conditions, using iron as an element enrichment carrier can form iron-based alloy type to achieve element enrichment, such as Mo [68].

2. Simulating Geochemical Environments of Ore Formation

First, it is necessary to identify the main minerals of the element in nature. Based on mineralogical information of the element carrier minerals, the geochemical environments of ore formation can be determined. In spite of the geochemical environment of element ore formation is difficult to simulate during application, the partial environmental characteristic of temperature, melt acidity/basicity, slag composition, and redox conditions during the element ore formation process can be simulated through pyrometallurgical methods. In terms of compositional design, in addition to determining the multi-component basicity, the addition of appropriate non-metallic elements to the slag may increase or decrease the migration rate of elements in the melt, indirectly achieving element enrichment. For example, rare earth elements (REEs) migrate more efficiently in fluids when the slag is in the condition of sulfate-rich [69].

In geochemistry, according to the different main components in magma, the types of magma deposit mainly include ultramafic rocks [70], carbonatites [71], alkaline rocks [72,73], etc. For example, alkaline rocks contain a high total alkali content (K_2O + Na_2O), and alkaline rocks are enriched in large ion lithophile elements (Ba and Rb), high field strength elements (Y, Zr, and Nb), and rare earth elements (REEs). Although the geochemical behavior of ore formation in magma cannot provide accurate guidance for EnAMs, it can provide research directions during the design process. For example, when designing engineered artificial niobium-bearing minerals (EnANMs), niobium mainly exists in the form of pyrochlore minerals, and pyrochlore is a common mineral in carbonatite and alkaline rock magma mineralization [74]. Generally, pyrochlore can locally accumulate in large quantities in carbonatite-alkaline rocks. Therefore, it can be determined that the ore-forming environment of pyrochlore is related to the alkalinity of the melt. In the study of pyrochlore solubility, pyrochlore group minerals are more common in peralkaline granite systems, while columbite is in peraluminous systems [75]. This is mainly because the solubility of pyrochlore in magma changes with the ratio of Al_2O_3/CaO+Na_2O+K_2O (A/CNK). The change in A/CNK value is basically consistent with the change in basicity in the melt. In the actual niobium concentrate conversion process, the transformation of niobium into EnANMs with perovskite or pyrochlore crystal structures can be achieved by controlling the content of alkaline oxides and acidic oxides in the slag [76]. In addition, according to the element composition of natural pyrochlore group minerals, the high field strength elements Nb, Ta, and Ti have similarities in the distribution of mineral types [77–79]. Similar crystallization behavior and migration paths may appear during the crystallization of the Nb, Ta, and Ti containing slag multi-element system. The geochemistry behaviors of pyrochlore group in different compositions in Figure 5 show that betafite exists in low Nb/Ti ratio and pyrochlore exists in high Nb ratio [77,80]. In the actual transformation behaviors in slag as shown in Figure 5b, as improving the Nb/Ti ratio of slag, the niobium-bearing phase transforms from calciobetafite to pyrochlore [81]. In addition, Thomas Schirmer et al. studied Ta and Ti containing slag and found that the behavior of Ta in synthetic slag was similar to that of Ti [30]. Ta and Ti are enriched in the corresponding perovskite. This result also illustrates that the crystallization behavior of some elements is similar with geochemical behavior. There are few cases of designing artificial minerals by simulating ore-forming geochemical environments, and further research is still needed to discover the connections and differences between EnAMs crystallization and nature ore-forming processes.

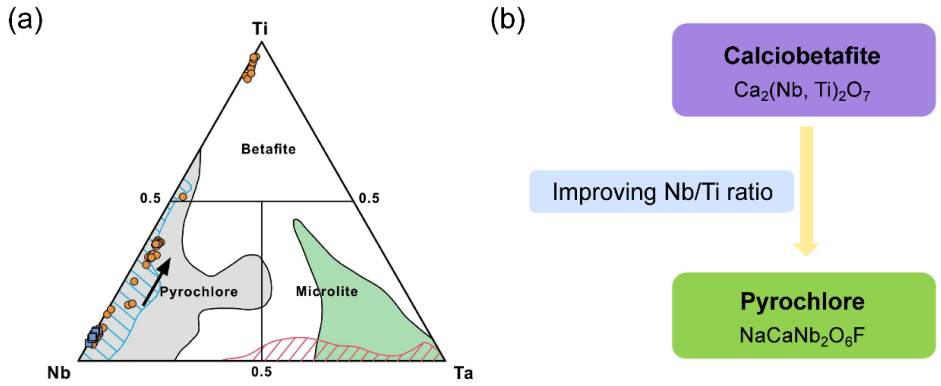

Figure 5. (**a**) The compositions of Pyrochlore-group minerals with different elements, including Nb, Ti, Ta (Reproduced with permission from [80], published by Elsevier B.V., 2021); (**b**). Phase transformation relationship bewteen calciobetafite and pyrochlore in slag.

4. Applications and Case Studies

4.1. Challenging Niobium Resources

The Bayan Obo niobium resource is characterized by a wide variety of niobium-bearing minerals, complex intergrowth relationships, and fine mineral particle size [82–86]. However, the complex mineralogical properties have hindered the efficient development and utilization of niobium through conventional physical beneficiation processes and equipment [87]. The Nb_2O_5 grade of the Bayan Obo low-grade niobium rougher concentrate can only be increased from 0.1%–0.2% to 1%–5% via physical beneficiation [87]. Addressing the challenge of inefficient development and utilization of the Bayan Obo niobium resources, a novel three-step combined beneficiation and metallurgy approach of "selective and precise pre-concentration, mineral phase transformation, industrial-scale EnAMs enrichment" has been proposed to overcome the mineralogical complexity. Firstly, to enhance the niobium grade, the raw materials are pre-enriched to obtain low-grade niobium rougher concentrate. Then, the low-grade niobium rougher concentrate undergoes mineral phase transformation, converting various niobium-bearing minerals into engineered artificial niobium-bearing minerals (EnANMs). Finally, the transformed slag containing EnANMs is crushed and enriched through beneficiation to achieve the utilization of niobium resources.

To clarify the crystallization behavior of niobium-bearing slag during the cooling process, the CaO-SiO_2-Nb_2O_5-La_2O_3 multi-component system was designed for optimizing slag design [88–94]. $CaNb_2O_6$, $LaNbO_4$, $Ca_2Nb_2O_7$, and the liquid phase are the main carriers of niobium after mineral phase transformation. $CaNb_2O_6$ preferentially precipitates in the low La_2O_3 region and under high CaO/SiO_2 ratio conditions. $Ca_2Nb_2O_7$ is stable at 1200 °C with medium CaO content. To further clarify the crystallization behavior of niobium in the slag under multi-component conditions, Lifeng Sun et al. conducted research on the CaO-SiO_2-Nb_2O_5-Fe_2O_3-TiO_2 five-component phase diagram at 1100 °C and 1200 °C, respectively [95,96]. At 1200 °C, the coexistence of $CaTiO_3$ and $Ca_{10}Nb_2Si_6O_{27}$ is dominant. At 1100 °C, a large amount of $CaSiO_3$ phase precipitates, inhibiting the formation of $CaTiO_3$. The influences of TiO_2 on the precipitates of niobium-bearing phase can be obtained. TiO_2 competes with Nb_2O_5 to enter the perovskite ($CaTiO_3$) phase, forming a $Ca(Ti,Nb)O_3$ solid solution. In addition, niobium partially transfers to $Ca_2Nb_2O_7$. Multi-component phase equilibrium studies have revealed that the crystallized niobium minerals after phase equilibrium mainly include perovskite structure, pyrochlore structure, and liquid phase.

Based on the theoretical foundation of phase equilibrium, Zhang Bo et al. conducted a mineral phase reconstruction study on Bayan Obo tailings by controlling the cooling crystallization method after high-temperature smelting reduction [97,98]. After carbothermal

smelting reduction in Bayan Obo tailings at 1600 °C, the iron forms spherical iron beads, which are completely separated from the slag. After smelting reduction crystallization regulation of Bayan Obo tailings at 1600 °C, perovskite, geikielite, forsterite precipitated in the slag as shown in Figure 6a [98]. Through elemental distribution analysis, Nb, Ti and REEs are enriched in perovskite. Nb-bearing minerals including niobite, pyrochlore, and bastnaesite in the tailings were mainly transformed into perovskite phase. REEs bearing minerals, including pyrochlore, aeschynite, and bastnaesite, were transformed into perovskite and geikielite. The distribution rates of Nb, REEs, and Ti in the perovskite phase are 94.52%, 63.10%, and 48.82%, respectively. In addition, during the solidification and crystallization process of silicon-iron bath smelting reduction, a large amount of perovskite precipitates from niobium-containing slag, and rare earth elements are also dissolved in the perovskite [99]. By adjusting w(CaO)/w(SiO_2) ratio in the range of 1.2–1.9 in the slag and maintaining the slag at 1100 °C for 4 h, the area fraction of perovskite in the final slag exceeds 37%. Mineral phase reconstruction transforms complex and diverse niobium mineral phases into REEs-bearing EnANMs.

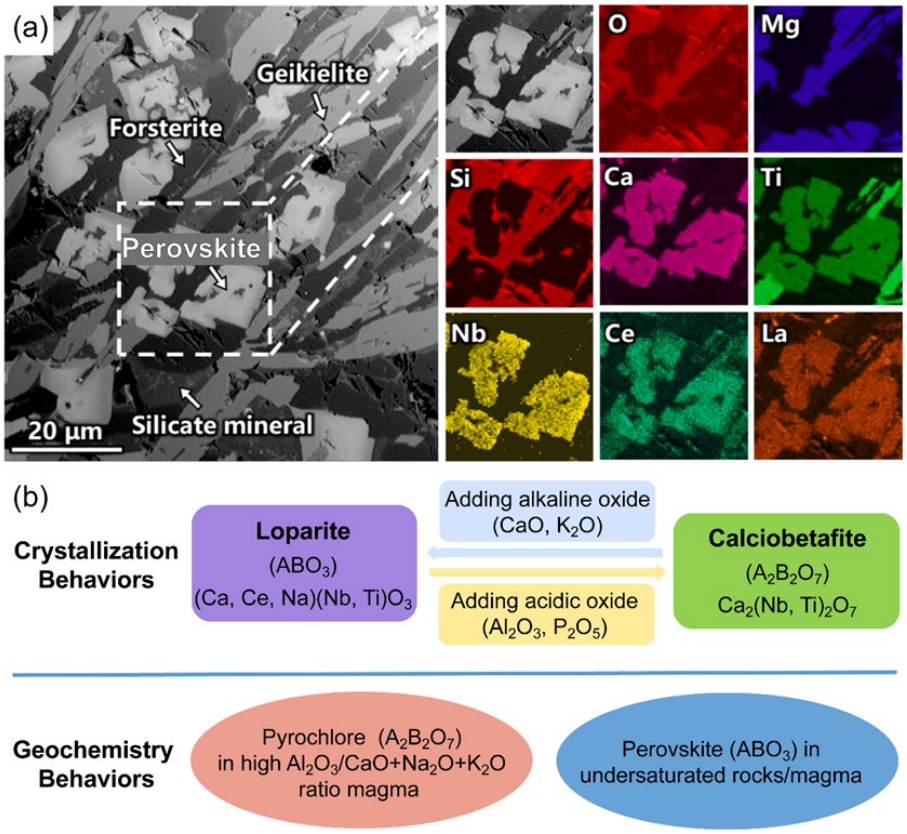

Figure 6. (**a**) SEM images of Bayan Obo tailings after carbothermic smelting reduction and crystallization control quenching [98], (**b**) the Crystallization behaviors of Nb-bearing phases in slag and the geochemistry behaviors of Nb-bearing minerals in magma.

Except applying phase diagrams in the reconstruction of Nb-bearing resources, simulating geochemical environments of ore formation was also applied. In the geochemistry behaviors of niobium-bearing minerals as shown in Figure 6b, the pyrochlore formed in the magma with high Al_2O_3/CaO+Na_2O+K_2O (A/CNK) ratio [75]. Perovskite exists in the undersaturated SiO_2 rocks or magmas [100]. Hencn, pyrochlore and perovskite form in different content of acidic oxides and alkaline oxides. In the crystallization behaviors study of Nb-bearing phases in slag, Wensheng Han et al. conducted mineral phase transformation research on pre-selected low-grade niobium rougher concentrate

through high-temperature smelting-cooling crystallization process [76]. Under an oxygen atmosphere, the transformed iron is present in the form of hematite and pseudobrookite; the transformed niobium is present in the form of loparite (perovskite structure) or calciobetafite (pyrochlore structure). As shown in Figure 6b, the niobium-bearing phase is transformed from calciobetafite to loparite by adding alkaline oxides (such as CaO, K_2O) to increase the slag basicity. For example, when the CaO/SiO_2 ratio increases from 0.5 to 1.4, the niobium-bearing phase in the slag changes from calciobetafite to loparite. By adding acidic oxides (such as Al_2O_3, P_2O_5) to decrease the slag basicity, the transformation of the niobium-bearing phase from loparite to calciobetafite is observed. For example, after adding 10% Al_2O_3 or P_2O_5, the diffraction peak intensity of loparite decreases, while the diffraction peak of calciobetafite appears despite the CaO/SiO_2 ratio is 1.4. The effect of slag basicity on niobium-bearing phase is consistent with the A/CNK value change in natural pyrochlore in the mineralization environment. Basicity regulation in slag can realize the directional transformation of various niobium minerals to calciobetafite (pyrochlore structure) and loparite (perovskite structure) [76]. The niobium content in different niobium-bearing phases varies with the change in basicity. The niobium content in the calciobetafite phase formed at lower basicity is relatively high. The mass fraction of Nb_2O_5 in calciobetafite reach 29.38%, and the total mass fraction of TiO_2, Nb_2O_5, and rare earth oxides (REO) in calciobetafite phase is 71.94%. The niobium content in the loparite phase formed at higher basicity is relatively low, and the mass fraction of Nb_2O_5 in loparite is 21.02%. Obviously, designing calciobetafite as EnAMs is more conducive to Nb enrichment. By studying the growth behavior of calciobetafite at different temperatures, a cooling process for EnAMs was designed [101]. When the melt is kept at 1245 °C for 3 h, calciobetafite does not crystallize, and hematite and pseudobrookite crystallize. When the temperature was maintained at 1200~1230 °C is beneficial to the growth of calciobetafite, and the temperature at 1140~1170 °C is beneficial to the nucleation of calciobetafite. During the cooling process of the melt, the maximum equivalent diameter of calciobetafite reaches 98.01 μm, which fulfills the granularity requirement for subsequent beneficiation.

4.2. Secondary Lithium Resource Recycling

When pyrometallurgical techniques are used to recover metals from secondary sources, such as lithium, nickel, and cobalt from spent batteries, these metals are reduced thermodynamically and hence separated from the slag by density [102,103]. However, lithium can not be separated and recovered because lithium has high oxygen affinity, consequently remaining in the slag [104]. Thomas Schirmer et al. conducted research on the design and control of EnAMs in lithium-containing slag systems, employing phase equilibrium design and calculations to study lithium-bearing EnAMs as enrichment carriers [45,105]. The primary lithium-bearing EnAMs includes lithium aluminate ($LiAlO_2$), spinel, lithium aluminum silicates, and calcium aluminum silicates. Among them, $LiAlO_2$ preferentially crystallizes at high temperatures, enabling efficient lithium enrichment; the crystal morphology (isometric crystals) of $LiAlO_2$ facilitates subsequent flotation separation [106,107]. And $LiAlO_2$ has the highest lithium content, approximately 10.5 wt%, which makes it a suitable lithium artificial mineral. In the study of the influence of components on $LiAlO_2$ crystallization, the increase in Mg/Al ratio promotes the preferential crystallization of high-melting-point spinel, leading to a reduction in $LiAlO_2$ crystallization, then affecting the distribution of Li in the minerals [45]. If the melt contains phosphorus, it may lead to the formation of Li_3PO_4 and inhibit the crystallization of lithium aluminate ($LiAlO_2$) [105]. Therefore, low-phosphorus and low-MgO content systems are the preferable designs to achieve efficient lithium enrich in $LiAlO_2$.

During the recovery lithium from $Li(Co_{1-x-y}Ni_xMn_y)O_2$ electrode materials, Alena Wittkowski et al. designed a Li_2O-CaO-SiO_2-Al_2O_3-MgO-MnO_x system to simulate slag and investigate the influence of manganese on the formation of lithium aluminate ($LiAlO_2$) [43]. Manganese in the slag is enriched in the form of spinel solid solutions $(Li_{2x}Mn^{2+}{}_{1-x})_{1+x}(Al_{2-z}, Mn^{3+}{}_z)O_4$. The enrichment of partial lithium and aluminum in spinel solid solution results in the decrease of $LiAlO_2$ crystallization. D.A. Abrue et al. designed a multi-element phase equilibrium study to reduce the formation of $LiMn_2O_4$ [108]. By employing the CALPHAD method and combining phase diagram data from binary/ternary systems (such as CaO-SiO_2, Li_2O-SiO_2, Li_2O-MnO_x, MnO_x-SiO_2), a thermodynamic database for multi-component systems can be established to predict phase equilibrium and crystallization paths. By controlling the oxygen partial pressure and cooling path of the slag, the precipitation of Li_2SiO_3 (high lithium content) and $LiMnO_2$ can be directionally controlled. Effective suppression of Lithium Manganate ($LiMn_2O_4$) promotes lithium enrichment in EnAMs.

In the overall process of EnAMs design, dissociation, and separation, Hao Qiu et al. used thermodynamic calculations to design and control lithium-bearing EnAMs in the Li_2O-CaO-Al_2O_3-SiO_2-MnO system, promoting lithium enrichment in the γ-$LiAlO_2$ phase and inhibiting its dispersion in other mineral phases as shown in Figure 7 [46]. The slag is cooled and crystallized, followed by beneficiation and leaching to recover lithium. Through the design and control of the slag, the mass fraction of γ-$LiAlO_2$ phase was 27.4%. And other lithium-bearing phase, the mass fractions of β-eucryptite (β-$LiAlSiO_4$) and lithium manganese silicate (Li_2MnSiO_4) in slag are only 2.2% and 3.8%, respectively. The lithium mainly enriches in γ-$LiAlO_2$, and the remainder enriches in β-eucryptite (β-$LiAlSiO_4$) and lithium manganese silicate (Li_2MnSiO_4). Some lithium may be distributed in the amorphous glass phase. After crushing and dissociating the cooled slag, flotation was performed [108]. The flotation process uses sodium oleate (NaOl) as a collector and sodium hexametaphosphate (SHMP) as a depressant for separation. A lithium concentrate with a grade of 10.94% Li_2O and a recovery rate of 30.45% were obtained. In addition, Sophie Acker et al. designed a novel imidazole-2-thione reagent for lithium aluminate ($LiAlO_2$) [109]. The recovery rates of $LiAlO_2$ and spodumene are 88.9% and 71.8%, respectively. While the recovery rate of gehlenite gangue was less than 15%, which demonstrates excellent selectivity for EnAMs. Future research and application of new reagents might better enable the recovery of Li-bearing EnAMs.

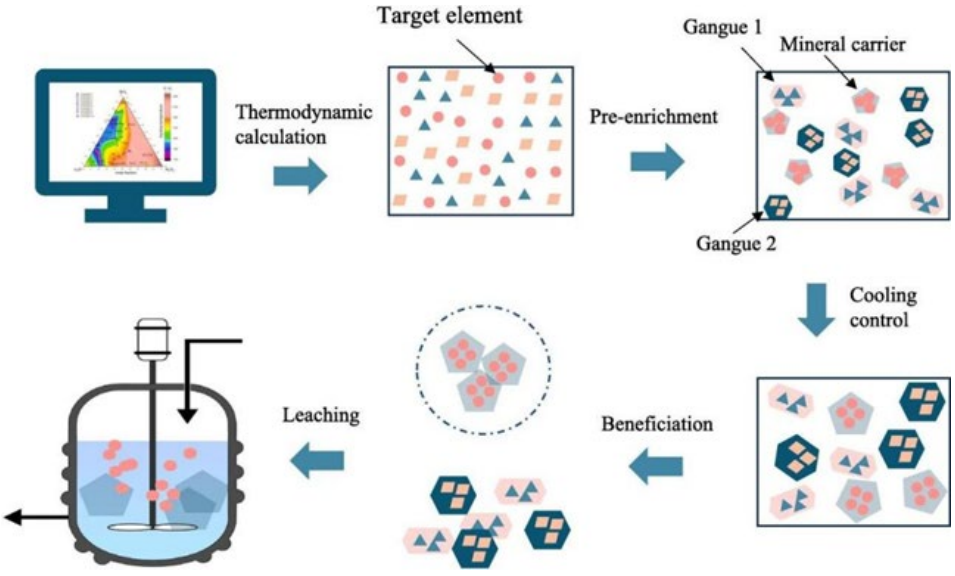

Figure 7. Schematic sketch of the overall process of EnAMs design, dissociation, and separation [46].

Except using the flotation method for mineral separation, Javadi and co-workers also employed electrostatic separation to separate lithium aluminate from mixed powders [31]. The enrichment of lithium aluminate can be significantly improved when the proportion of particles with high free surface area values increases.

4.3. Recovery and Crystallization of Rare Earth from Slag

The recovery of Ce and La from rare earth slags is primarily achieved through mainstream recovery processes including hydrometallurgy, electrochemistry, bio-hydrometallurgy, and pyrometallurgy. Among them, promoting innovation in high-temperature recovery technologies can foster the sustainable recovery and utilization of rare earth resources [110]. The high-temperature melting-cooling crystallization method can be used to construct engineered artificial rare earth elements-bearing phases in the slag.

To study the crystallization behaviors of REEs in slag, the phase equilibrium relationships of multi-component systems such as CaO-SiO_2-La_2O_3 [111], CaO-SiO_2-Al_2O_3-Ce_2O_3 [112,113], CaO-SiO_2-CaF_2-Ce_2O_3 [114], CaO-SiO_2-CeO_2-10.0 wt% Al_2O_3-5.0 wt% MgO [115], and CaO–SiO_2–CaF_2(30 wt%)-P_2O_5(10 wt%)-Ce_2O_3 [49] at different temperatures have been widely studied. Researchers have revealed that the main rare earth element-bearing phases include $Ca_xLa_{4.67-x}(SiO_4)_3O_{1-0.5x}$ (containing 70 wt% La_2O_3), $La_2Ca_3(SiO_3)_6$ (containing 40 wt% La_2O_3), $Ce_{4.667-x}Ca_x(SiO_4)_3O_{1-0.5x}$, $Ce_{9.33-x}Ca_x(SiO_4)_4O_{5-0.5x}F_2$, $Ca_5(PO_4)_3F$, and silicophosphate apatite ($Ca_{5-x}Ce_x[(Si,P)O_4]_3F$). Because the $Ca_xLa_{4.67-x}(SiO_4)_3O_{1-0.5x}$, $Ce_{4.667-x}Ca_x(SiO_4)_3O_{1-0.5x}$, britholite-(Ce), silicophosphate apatit, and $Ca_5(PO_4)_3F$ phases have a high content of REEs, these phases are potential candidate EnAMs. According to the phase equilibrium results, it is promising to design an environment where only rare earth element-bearing phases are preferentially precipitated in the liquid phase [114,116]. As shown in Figure 8a, only the $Ce_{9.33-x}Ca_x(SiO_4)_4O_{5-0.5x}F_2$ phase forms in zoon 9. Then rare earth element-bearing phases can be extracted by solid–liquid separation technology.

Further research on the crystallization behavior of rare earth element-bearing phases has revealed that the crystallization model is mainly diffusion-controlled [116–118]. The crystallization model suggests the cooling rate of slag should be in the range of 20–30 °C/min [116]. Regarding the growth behavior of rare earth element-bearing EnAMs, an increase in P_2O_5 content shortens the incubation time of EnAMs because P_2O_5 raises the initial crystallization temperature [118]. The P_2O_5 also can increase the nucleation rate because it reduces the activation energy for crystallization [118]. Hence, P_2O_5 can promote the growth of rare earth element-bearing EnAMs in certain conditions [119]. In addition, P_2O_5 content also affects the transformation of apatite ($Ca_{2.02}Ce_{7.98}Si_6O_{26}$) and britholite ($Ca_{5-x}Ce_x[(SiO_4)_x(PO_4)_{3-x}]F$) [117]. Conversely, increasing the CaF_2 content in slag has the opposite effect on incubation time and nucleation rate compared to phosphorus [118].

In a separation method for REEs, Xi Lan et al. used centrifugal force generated by rotation to separate and recover REEs from the slag system because of the density difference between rare earth element-bearing EnAMs and slag, as shown in Figure 8b [120]. In the centrifugal equipment, a counterweight and a heating furnace are symmetrically fixed on the centrifugal rotor. The heating furnace continuously heats during the rotation process to stabilize the temperature. After the separation process, the rare earth element-bearing EnAMs move to the bottom of the slag, as shown in Figure 8c. In Figure 8c, Cerium fluorosilicate (Ce_2O_3: 67.23 wt%) was selectively separated from the CaO-SiO_2-CaF_2-Ce_2O_3 system, achieving a rare earth recovery rate of 98.23% [120]. Similarly, britholite with varying Ce_2O_3 contents (17.87–46.93 wt%) was separated from the CaO-SiO_2-CaF_2-P_2O_5-Ce_2O_3 system, with rare earth recovery rates reaching 95.58%–98.65% [121]. In the practical application of Bayan Obo rare earth concentrate, the major rare earth elements (Ce, La, Pr, and Nd) were enriched in EnAMs as the temperature decreased. Cerium was almost entirely

transformed into the Ce-oxide phase, lanthanum was present in the La-ferrate phase, and praseodymium and neodymium were mainly enriched in apatite. After supergravity separation, the recovery rates of Ce in the Ce-oxide phase, La in the La-ferrate phase, and Pr and Nd in the apatite phase reached 98.80%, 96.81%, 92.12%, respectively [122].

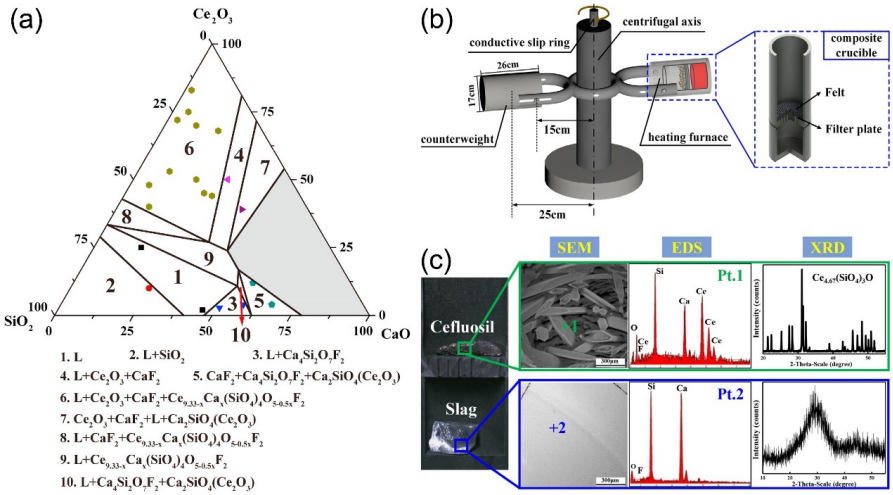

Figure 8. (**a**) Isothermal phase equilibria diagram of the CaO–SiO_2–CaF_2–Ce_2O_3 system at 1373 K with a fixed CaF_2 component (reproduced with permission from [114], published by Elsevier Ltd. and Techna Group S.r.l., 2020) All rights reserved. (**b**) Operation schematic illustrations of the centrifugal device [120], and (**c**) vertical section of the sample via supergravity and the corresponding results [120].

Current studies in phase diagram construction and crystallization kinetics analysis have clarified the formation mechanism and separation conditions of rare earth element-bearing EnAMs. Supergravity technology provides a new pathway for efficient recovery. However, the thermodynamic database for REE systems still needs improvement, and further research is needed on complex component interactions and non-equilibrium crystallization behavior. In the future, the combination of artificial intelligence and high-throughput experimental techniques can accelerate phase diagram prediction and promote the sustainable utilization of rare earth resources.

EnAM design is applied not only in REE slags but also in blast furnace titanium slag to design perovskite as an EnAM for titanium recovery [123–126]. In high-iron-content nickel slag/blast furnace slag, EnAMs such as (Ni,Fe)Fe_2O_4 [127], Magnetite [128–130], and (Mn,Mg)y$Fe_{3-y}O_4$ [67] are designed. Iron and associated elements, such as the Co, Ni, and Cu in EnAMs, can be recovered by magnetic separation. From stainless steel chromium slag, spinel EnAMs were designed for chromium immobilization [53,131,132]. In vanadium converter slag, V-bearing spinel EnAMs were designed for vanadium enrichment [133]. Therefore, most of the high-value elements and harmful elements in slag can be recovered and transformed by constructing EnAMs.

5. Challenges and Future Perspectives

5.1. Optimization of EnAMs Design

On the one hand, based on thermodynamic phase simulations and development of databases for the mineralogical phases, the conversion rate of EnAMs should be enhanced. After slag cooling and crystallization, target elements are not only enriched in EnAMs but also in other gangue phases and amorphous glass phases, leading to difficulties in sorting various minerals and low recovery rates.

On the other hand, during EnAMs design, the magnetic, density, and dielectric properties of gangue should be considered. Gangue minerals that exhibit physical properties and differences relative to EnAMs facilitate subsequent mineral processing.

5.2. Improving Economic Viability

To achieve the separability of EnAMs after liberation, a relatively long cooling and crystallization time is required to ensure the particle size of EnAMs, which results in the low economic viability of the process. In the future, research should focus on the crystallization kinetics of the slag system, and additive engineering to promote the rapid growth of EnAMs. Designing new high-temperature conversion equipment powered by renewable electricity achieves the application of green electricity in EnAMs and improves economic viability.

5.3. Physical Separation of Fine-Grained (<20 μm) EnAMs

To reduce the cost of metal recovery processes, physical separation equipment for fine-grained minerals should be vigorously developed. If efficient separation of fine-grained minerals can be achieved based on magnetic, density, or conductivity differences, it will greatly reduce the crystallization time during slag cooling. Thereby, effective physical separation improves economic viability while reducing the environmental pollution caused by flotation or leaching processes.

6. Conclusions

Constructing engineered artificial minerals (EnAMs) is an effective strategy for sustainable resource recovery from complex mineral resources, metallurgical waste slags, and secondary urban mines. By leveraging high-temperature phase reconstruction processes, EnAMs enable the selective enrichment of target elements (e.g., Nb, REEs, Li, Cr, and V) into designed crystalline phases during crystallization melting. In comparison, phase equilibrium studies are more effective and scientific than utilizing geochemical behaviors when designing EnAMs. However, in certain specific cases, the metallogenic geochemical behavior of elements can also provide rough guidance for EnAM design. The limitations of geochemical behaviors in phase reconstruction highlight the need for further exploration of the relationship study between geochemistry and pyrometallurgy. The application of EnAMs in metal recovery from complex resources has achieved some success. During the transformation process, target elements can be enriched selectively in EnAMs. However, further research is still needed on the design, dissociation, and beneficiation of EnAMs. In the future, electricity generated from new energy sources can be applied to the energy required for preheating and cooling in the process of mineral phase reconstruction. This will provide a clean approach for the mineral phase reconstruction of complex resources. Overall, designing EnAMs to solve the development of complex resources has broad prospects.

Author Contributions: Conceptualization, W.H., W.C. and B.F.; data curation, W.H.; writing—original draft preparation, W.H.; writing—review and editing, W.H., J.W., X.L., D.M., C.J., H.L., M.R., W.C. and B.F.; supervision, W.C. and B.F.; funding acquisition, W.H., X.L., W.C. and B.F. All authors have read and agreed to the published version of the manuscript.

Funding: This study is supported by the Ministry of Science and Technology of the People's Republic of China (Young Scientist Program, Grant No. 2021YFC2901200), China Minmetals Corporation (Youth Science and Technology Fund, Grant No. 2024QNJJB26) and the National Natural Science Foundation of China within the Priority Projects "Mineral phases transformation and enrichment utilization of Bayan Obo complex niobium depos-it in artificial geochemical microenvironment" (Grant No. 92062223), and the German Research Foundation within the priority program "Engineered

Artificial Minerals (EnAM)—a geo-metallurgical tool to recycle critical elements from waste streams" (SPP 2315, Grant No. 470553874).

Data Availability Statement: No new data were created or analyzed in this study.

Acknowledgments: The authors from Changsha Research Institute of Mining and Metallurgy Co., Ltd. acknowledge the funding support from the Ministry of Science and Technology of the People's Republic of China (Young Scientist Program, Grant No. 2021YFC2901200), China Minmetals Corporation (Youth Science and Technology Fund, Grant No. 2024QNJJB2), and the National Natural Science Foundation of China within the Priority Projects "Mineral phases transformation and enrichment utilization of Bayan Obo complex niobium depos-it in artificial geochemical microenvironment"(Grant No. 92062223). The authors from RWTH Aachen University acknowledge the financial support of the German Research Foundation within the priority program "Engineered Artificial Minerals (EnAM)—a geo-metallurgical tool to recycle critical elements from waste streams" (SPP 2315, Grant No. 470553874). The authors from RWTH Aachen University additionally acknowledge the coordination by Urs Peuker from the Institute of Mechanical Process Engineering and Mineral Processing, TU Bergakademie University.

Conflicts of Interest: Wensheng Han, Xiang Lu, Chuling Jiang, Mengjie Ran and Wen Chen are employees of Changsha Research Institute of Mining and Metallurgy Co., Ltd. The authors declare that they have no known competing financial interests or personal relationships that could have appeared to influence the work reported in this paper.

Abbreviations

The following abbreviations are used in this manuscript:

EnAMs	Engineered Artificial Minerals
EnANMs	Engineered Artificial Niobium-Bearing Minerals
HEV	Hybrid Electric Vehicle
PGMs	Platinum-Group Metals
REEs	Rare Earth Elements
WEEE	Electrical and Electronic Equipment Waste

References

1. Li, Z.; Wang, C.; Chen, J. Supply and demand of lithium in China based on dynamic material flow analysis. *Renew. Sustain. Energy Rev.* **2024**, *203*, 114786. [CrossRef]
2. Tang, H.; Peng, Z.; Tian, R.; Ye, L.; Zhang, J.; Rao, M.; Li, G. Platinum-group metals: Demand, supply, applications and their recycling from spent automotive catalysts. *J. Environ. Chem. Eng.* **2023**, *11*, 110237. [CrossRef]
3. Pan, D.; Yuming, C.; Jinhua, Y.E.; Weibo, Z. Study on the resource distribution and industry development of global niobium and tantalum. *China Min. Mag.* **2019**, *28*, 63–68.
4. Mackay, D.A.R.; Simandl, G.J. Geology, market and supply chain of niobium and tantalum—A review. *Miner. Depos.* **2014**, *49*, 1025–1047. [CrossRef]
5. Zhu, Z.; Wang, D.; Li, Y.; Ke, C.; Yu, H.; Chen, Z.; She, H.; Wang, R.; Hu, H.; Zhao, Y.; et al. Detail mineralogical study and geochronological framework of Bayan Obo (China) Nb mineralization recorded by in situ U-Pb dating of columbite. *Ore Geol. Rev.* **2024**, *165*, 105874. [CrossRef]
6. Rene, E.R.; Sethurajan, M.; Kumar Ponnusamy, V.; Kumar, G.; Bao Dung, T.N.; Brindhadevi, K.; Pugazhendhi, A. Electronic waste generation, recycling and resource recovery: Technological perspectives and trends. *J. Hazard. Mater.* **2021**, *416*, 125664. [CrossRef]
7. Shahabuddin, M.; Uddin, M.N.; Chowdhury, J.I.; Ahmed, S.F.; Uddin, M.N.; Mofijur, M.; Uddin, M.A. A review of the recent development, challenges, and opportunities of electronic waste (e-waste). *Int. J. Environ. Sci. Technol.* **2023**, *20*, 4513–4520. [CrossRef]
8. Botelho, A.B., Jr.; da Silva, M.; Camargo, P.S.S.; Munchen, D.D.; Cenci, M.P.; Bertuol, D.A.; Veit, H.M.; Tenório, J.A.S.; Espinosa, D.C.R. Electronic waste in emerging countries: Current scenario of generation, policies, and recycling technologies regarding the coronavirus pandemic. *Int. J. Environ. Sci. Technol.* **2024**, *21*, 1121–1140. [CrossRef]
9. Li, P.W.; Luo, S.H.; Zhang, L.; Liu, Q.Y.; Wang, Y.K.; Lin, Y.C.; Xu, C.; Guo, J.; Cheali, P.; Xia, X.N. Progress, challenges, and prospects of spent lithium-ion batteries recycling: A review. *J. Energy Chem.* **2024**, *89*, 144–171. [CrossRef]

10. Abdalla, A.M.; Abdullah, M.F.; Dawood, M.K.; Wei, B.; Subramanian, Y.; Azad, A.T.; Nourin, S.; Afroze, S.; Taweekun, J.; Azad, A.K. Innovative lithium-ion battery recycling: Sustainable process for recovery of critical materials from lithium-ion batteries. *J. Energy Storage* **2023**, *67*, 107551. [CrossRef]
11. Sun, S.; Jin, C.; He, W.; Li, G.; Zhu, H.; Huang, J. A review on management of waste three-way catalysts and strategies for recovery of platinum group metals from them. *J. Environ. Manag.* **2022**, *305*, 114383. [CrossRef]
12. Xolo, L.; Moleko-Boyce, P.; Makelane, H.; Faleni, N.; Tshentu, Z.R. Status of recovery of strategic metals from spent secondary products. *Minerals* **2021**, *11*, 673. [CrossRef]
13. Swain, B. Recovery and recycling of lithium: A review. *Sep. Purif. Technol.* **2017**, *172*, 388–403. [CrossRef]
14. Kaya, M. Recovery of lithium from secondary resources. *Chem. Eng. Prog.* **2024**, *120*, 55.
15. Hagelüken, B.C. Recycling the platinum group metals: A european perspective. *Platin. Met. Rev.* **2012**, *56*, 29–35. [CrossRef]
16. Yakoumis, I.; Moschovi, A.M.; Giannopoulou, I.; Panias, D. Real life experimental determination of platinum group metals content in automotive catalytic converters. *IOP Conf. Ser. Mater. Sci. Eng.* **2018**, *329*, 012009. [CrossRef]
17. Korkmaz, K.; Alemrajabi, M.; Rasmuson, Å.; Forsberg, K. Recoveries of valuable metals from spent nickel metal hydride vehicle batteries via sulfation, selective roasting, and water leaching. *J. Sustain. Metall.* **2018**, *4*, 313–325. [CrossRef]
18. Meshram, P.; Somani, H.; Pandey, B.D.; Mankhand, T.R.; Deveci, H. Two stage leaching process for selective metal extraction from spent nickel metal hydride batteries. *J. Clean. Prod.* **2017**, *157*, 322–332. [CrossRef]
19. El Ouardi, Y.; Virolainen, S.; Massima Mouele, E.S.; Laatikainen, M.; Repo, E.; Laatikainen, K. The recent progress of ion exchange for the separation of rare earths from secondary resources—A review. *Hydrometallurgy* **2023**, *218*, 106047. [CrossRef]
20. Firdaus, M.; Rhamdhani, M.A.; Durandet, Y.; Rankin, W.J.; McGregor, K. Review of high-temperature recovery of rare earth (Nd/Dy) from magnet waste. *J. Sustain. Metall.* **2016**, *2*, 276–295. [CrossRef]
21. Holuszko, M.E.; Kumar, A.; Espinosa, D.C.R. *Electronic Waste: Recycling and Reprocessing for a Sustainable Future*; Wiley-VCH GmbH: Weinheim, Germany, 2022.
22. Menad, N.; Kana, N.; Kanari, N.; Pereira, F.; Seron, A. Process for enhancing the valuable metal recovery from "electric arc furnace" (EAF) slags. *Waste Biomass Valorization* **2021**, *12*, 5187–5200. [CrossRef]
23. Vuppaladadiyam, S.S.V.; Thomas, B.S.; Kundu, C.; Vuppaladadiyam, A.K.; Duan, H.; Bhattacharya, S. Can e-waste recycling provide a solution to the scarcity of rare earth metals? An overview of e-waste recycling methods. *Sci. Total Environ.* **2024**, *924*, 171453. [CrossRef] [PubMed]
24. Tawonezvi, T.; Nomnqa, M.; Petrik, L.; Bladergroen, B.J. Recovery and recycling of valuable metals from spent lithium-ion batteries: A comprehensive review and analysis. *Energies* **2023**, *16*, 1365. [CrossRef]
25. Critical Raw Materials Resilience: Charting a Path Towards Greater Security and Sustainability. Available online: https://www.eesc.europa.eu/en/our-work/opinions-information-reports/opinions/critical-raw-materials-resilience-charting-path-towards-greater-security-and-sustainability (accessed on 24 March 2021).
26. Generation of Electronic Waste Worldwide in the Years from 2014 to 2019 and a Forecast Until 2030. Available online: https://de.statista.com/statistik/daten/studie/792541/umfrage/erzeugung-von-elektroschrott-weltweit/ (accessed on 31 July 2020).
27. Latacz, D.; Diaz, F.; Birich, A.; Flerus, B.; Friedrich, B. WEEE recycling at IME – RWTH Aachen: From basic metal recovery to resource efficiency. *World Metall. Erzmetall* **2020**, *3*, 155–162.
28. Ji, R.; Liu, T.-J.; Kang, L.-L.; Wang, Y.-T.; Li, J.-G.; Wang, F.-P.; Yu, Q.; Wang, X.-M.; Liu, H.; Guo, H.-W.; et al. A review of metallurgical slag for efficient wastewater treatment: Pretreatment, performance and mechanism. *J. Clean. Prod.* **2022**, *380*, 135076. [CrossRef]
29. Rachmawati, C.; Weiss, J.; Lucas, H.I.; Löwer, E.; Leißner, T.; Ebert, D.; Möckel, R.; Friedrich, B.; Peuker, U.A. Characterisation of the grain morphology of artificial minerals (EnAMs) in lithium slags by correlating multi-dimensional 2D and 3D methods. *Minerals* **2024**, *14*, 130. [CrossRef]
30. Schirmer, T.; Hiller, J.; Weiss, J.; Munchen, D.; Lucas, H.; Fittschen, U.E.A.; Friedrich, B. Behavior of tantalum in a Fe-Dominated synthetic fayalitic slag system—Phase analysis and incorporation. *Minerals* **2024**, *14*, 262. [CrossRef]
31. Javadi, M.; Rachmawati, C.; Wollmann, A.; Weiss, J.; Lucas, H.; Möckel, R.; Friedrich, B.; Peuker, U.; Weber, A.P. Enhancing lithium recovery from slag through dry forced triboelectric separation: A sustainable recycling approach. *Minerals* **2024**, *14*, 1254. [CrossRef]
32. Dohrn, R.; Fonseca, J.M.S.; Peper, S. Experimental methods for phase equilibria at high pressures. *Annu. Rev. Chem. Biomol. Eng.* **2012**, *3*, 343–367. [CrossRef]
33. Xu, K.; Zhan, C.C.; Lou, M.; Xiao, X.L.; Zhou, R.A.; Wang, F.M.; Hu, X.F.; Yuan, Y.; Chang, K.K. Design of the rare-earth-containing materials based on the micro-alloying phase equilibria, phase diagrams and phase transformations. *J. Mater. Sci. Technol.* **2023**, *151*, 119–149. [CrossRef]
34. Dimian, A.C.; Bildea, C.S.; Kiss, A.A. Phase equilibria. *Integr. Des. Simul. Chem. Process* **2014**, *35*, 201–251.
35. Lv, N.N.; Qiu, Y.C.; Hu, Y.M.; Shi, H.K.; Shi, J.J.; Ding, X.; Li, H.L. Equilibrium phase relationships of CaO-SiO_2-TiO_2 system with 5 wt% Cr_2O_3 addition for titania-bearing slag recycling. *J. Sustain. Metall.* **2023**, *9*, 1303–1314. [CrossRef]

36. Shi, J.J.; Chen, M.; Wan, X.B.; Taskinen, P.; Jokilaakso, A. Phase equilibrium study of the CaO-SiO_2-MgO-Al_2O_3-TiO_2 system at 1300 °C and 1400 °C in Air. *JOM* **2020**, *72*, 3204–3212. [CrossRef]
37. Chen, M.; Shi, J.J.; Taskinen, P.; Jokilaakso, A. Phase equilibria of the CaO-SiO_2-TiO_2-Al_2O_3-MgO system in air at 1250–1400 °C. *Ceram. Int.* **2020**, *46*, 27702–27710. [CrossRef]
38. Wang, Z.; Xu, R.Z. Phase equilibria of TiO_2-SiO_2-CaO-10% Al_2O_3-7.5% MgO at 1773 K and effects of MgO on the distribution of phase fields. *Ceram. Int.* **2024**, *50*, 29975–29986. [CrossRef]
39. Kaußen, F.; Friedrich, B. Reductive smelting of red mud for iron recovery. *Chem. Ing. Tech.* **2015**, *87*, 1535–1542. [CrossRef]
40. Wan, X.; Shi, J.; Klemettinen, L.; Chen, M.; Taskinen, P.; Jokilaakso, A. Equilibrium phase relations of CaO–SiO_2–TiO_2 system at 1400 °C and oxygen partial pressure of 10^{-10} atm. *J. Alloys Compd.* **2020**, *847*, 156472. [CrossRef]
41. Shi, J.J.; Qiu, Y.C.; Wan, X.B.; Yu, B.; Chen, M.; Zhao, F.; Li, J.Z.; Liu, C.S.; Taskinen, P. Equilibrium Phase Relations of the CaO-SiO_2-Ti_3O_5 System at 1400 °C and a p(O_2) of 10^{-16} atm. *JOM* **2022**, *74*, 668–675. [CrossRef]
42. Wan, X.; Chen, M.; Qiu, Y.; Shi, J.; Li, J.; Liu, C.; Taskinen, P.; Jokilaakso, A. Influence of manganese oxide on the liquid-perovskite equilibrium in the CaO–SiO_2–TiO_2 system at 1400 °C in air. *Ceram. Int.* **2021**, *47*, 11176–11182. [CrossRef]
43. Wittkowski, A.; Schirmer, T.; Qiu, H.; Goldmann, D.; Fittschen, U.E.A. Speciation of manganese in a synthetic recycling slag relevant for lithium recycling from lithium-ion batteries. *Metals* **2021**, *11*, 188. [CrossRef]
44. Fittschen, U.E.A.; Hampel, S.; Schirmer, T.; Merkert, N. Multimodal spectroscopy and molecular dynamic simulations to understand redox-chemistry and compound formation in pyrometallurgical slags: Example of manganese oxidation state with respect to lithium recycling. *Appl. Spectrosc. Rev.* **2024**, *59*, 780–797. [CrossRef]
45. Schirmer, T.; Qiu, H.; Li, H.; Goldmann, D.; Fischlschweiger, M. Li-distribution in compounds of the Li_2O-MgO-Al_2O_3-SiO_2-CaO System—A first survey. *Metals* **2020**, *10*, 1633. [CrossRef]
46. Qiu, H.; Li, H.; Fischlschweiger, M.; Ranneberg, M.; Graupner, T.; Lucas, H.; Stallmeister, C.; Friedrich, B.; Yagmurlu, B.; Goldmann, D. Valorization of lithium containing slags from pyrometallurgical recycling route of spent lithium-ion batteries: The enrichment of γ-$LiAlO_2$ phase from thermodynamic controlled and modified slags. *Miner. Eng.* **2024**, *217*, 108918. [CrossRef]
47. Li, Y.; Yan, B. Phase equilibria relationship in the FetO-TiO_2-CaO-SiO_2 system with CaO/SiO_2 weight ratio of 12 at, 1673 K. *Calphad* **2024**, *87*, 102768. [CrossRef]
48. Ma, H.; Jiao, K.; Zhang, J.; Zong, Y.; Zhang, J.; Meng, S. Viscosity of CaO-MgO-Al_2O_3-SiO_2-TiO_2-FeO slag with varying TiO_2 content: The Effect of Crystallization on Viscosity Abrupt Behavior. *Ceram. Int.* **2021**, *47*, 17445–17454. [CrossRef]
49. Lan, X.; Gao, J.T.; Li, Y.; Guo, Z.C. Phase equilibria of CaO-SiO_2-CaF_2-P_2O_5-Ce_2O_3 system and formation mechanism of britholite. *Ceram. Int.* **2021**, *47*, 11966–11972. [CrossRef]
50. Coquerel, G. Phase diagrams for process design. In *Engineering Crystallography: From Molecule to Crystal to Functional Form*; Roberts, K.J., Docherty, R., Tamura, R., Eds.; Springer: Berlin/Heidelberg, Germany, 2017; pp. 215–233.
51. Fan, Y.; Shibata, E.; Iizuka, A.; Nakamura, T. Crystallization behaviors of copper smelter slag studied using time-temperature-transformation diagram. *Mater. Trans.* **2014**, *55*, 958–963. [CrossRef]
52. Weiss, J.; Munchen, D.; Richter, S.; Friedrich, B. Crystallization study of a synthetic fayalitic slag system with ta based on thermochemical modeling. In Proceedings of the 63rd Conference of Metallurgists, COM 2024, Toronto, ON, Canada, 21–24 August 2024; Springer Nature: Cham, Switzerland, 2025; pp. 1361–1368.
53. Wu, S.-w.; Zhang, Y.-l.; Zhang, S. Chromium enrichment in different crystalline phases of Cr-containing slag under various basicities and equilibrium temperatures. *J. Iron Steel Res. Int.* **2022**, *29*, 1412–1422. [CrossRef]
54. Gibson, C.E.; Kelebek, S.; Aghamirian, M. Niobium oxide mineral flotation: A review of relevant literature and the current state of industrial operations. *Int. J. Miner. Process.* **2015**, *137*, 82–97. [CrossRef]
55. Qi, H.; Gong, N.; Zhang, S.-Q.; Li, J.; Yuan, G.-L.; Liu, X.-F. Research progress on the enrichment of gallium in bauxite. *Ore Geol. Rev.* **2023**, *160*, 105609. [CrossRef]
56. Guan, T.; Guo, M.; Wang, L.; Liu, J. Production and recycling of the cutting edge material of gallium: A review. *Sci. Total Environ.* **2025**, *971*, 179046. [CrossRef]
57. Mollo, S.; Hammer, J.E. Dynamic crystallization in magmas. In *Mineral Reaction Kinetics: Microstructures, Textures, Chemical and Isotopic Signatures*; Heinrich, W., Abart, R., Eds.; European Mineralogical Union and the Mineralogical Society of Great Britain & Ireland: London, UK, 2017; Volume 16, pp. 373–412.
58. Encyclopedia of Geochemistry: A comprehensive reference source on the chemistry of the earth. In *Encyclopedia of Geochemistry: A Comprehensive Reference Source on the Chemistry of the Earth*; White, W.M., Ed.; Springer International Publishing: Cham, Switzerland, 2018; pp. 1–1557.
59. Vance, D.; Little, S.H. The history, relevance, and applications of the periodic system in geochemistry. In *Periodic Table I: Historical Development and Essential Features*; Mingos, D.M.P., Ed.; Springer International Publishing: Cham, Switzerland, 2019; Volume 181, pp. 111–156.
60. Lei, Y.; Sun, F.; Zhao, Z. Interdisciplinarity of geochemistry and extractive metallurgy- Taking platinum group metals and gold as examples. *Chin. J. Nonferrous Met.* **2023**, *33*, 2957–2974.

61. Sun, F.L.; Zhao, Z.W. An interdisciplinary perspective from the earth scientist's periodic table: Similarity and connection between geochemistry and metallurgy. *Engineering* **2020**, *6*, 707–715. [CrossRef]
62. Volodin, V.; Trebukhov, S.; Nitsenko, A.; Linnik, X.; Tuleutay, F.; Trebukhov, A.; Ruzakhunova, G. Pyrometallurgical scheme intended to process arsenic-containing concentrates with recovery of precious metals. *Metals* **2023**, *13*, 540. [CrossRef]
63. Yu, B.Q.; Kou, J.; Sun, C.B.; Sun, F.; Gui, C.L.; Liu, J. Development of special magnetic separator to recover precious metal-bearing alloy from high-grade nickel matte and its magnetic field simulation. *Min. Metall. Explor.* **2022**, *39*, 1687–1692. [CrossRef]
64. Li, Z.C.; Tian, Q.H.; Wang, Q.M.; Guo, X.Y. Recovery of copper, lead and zinc from copper flash converting slag by the sulfurization-reduction process. *JOM* **2023**, *75*, 1107–1118. [CrossRef]
65. Liao, Y.L.; Ji, G.X.; Shi, G.C.; Xi, J.J. A study on the selective leaching of valuable metals and the configuration of iron silicon phases in copper smelting slag by oxidative pressure leaching. *J. Sustain. Metall.* **2021**, *7*, 1143–1153. [CrossRef]
66. Zhang, L.; Zhang, W.; Zhang, J.; Li, G. Oxidation kinetics and oxygen capacity of ti-bearing blast furnace slag under dynamic oxidation conditions. *Metals* **2016**, *6*, 105. [CrossRef]
67. Huang, L.; An, S.; Zhang, F.; Peng, J.; Chen, Y.; Ping, X.; Liu, C. Synergistic treatment of blast furnace slag and basic oxygen furnace slag for efficient recovery of iron: Phase transformation and oxidation mechanisms. *J. Mater. Res. Technol.* **2024**, *28*, 2347–2362. [CrossRef]
68. Long, T.V.; Palacios, J.; Sanches, M. Recovery of molybdenum from copper slag. *Tetsu Hagane-J. Iron Steel Inst. Jpn.* **2012**, *98*, 48–54. [CrossRef]
69. Fan, H.R.; Niu, H.C.; Li, X.C.; Yang, K.F.; Yang, Z.F.; Wang, Q.W. The types, ore genesis and resource perspective of endogenic REE deposits in China. *Chin. Sci. Bull.-Chin.* **2020**, *65*, 3778–3793. [CrossRef]
70. Lobach-Zhuchenko, S.B.; Baltybaev, S.K.; Egorova, Y.S.; Sergeev, S.A.; Kaulina, T.; Saltykova, T.E. Stages of paleoarchean to paleoproterozoic basic-ultrabasic magmatism in the sarmatian craton. *Russ. Geol. Geophys.* **2022**, *63*, 225–244. [CrossRef]
71. Raza, M.; Giebel, R.J.; Staude, S.; Beranoaguirre, A.; Kolb, J.; Markl, G.; Walter, B.F. The magmatic to post-magmatic evolution of the Nooitgedacht Carbonatite Complex, South Africa. *Geochemistry* **2025**, *85*, 126249. [CrossRef]
72. Emad, B.M. Alkaline igneous rocks, a potential source of rare metals and radioactive minerals: Case study at Amreit area, south Eastern Desert, Egypt. *Acta Geochim.* **2025**, *44*, 189–214. [CrossRef]
73. Xi, Z.-C.; Qiu, K.-F.; Zhi, C.-L.; Li, S.-S.; Shang, Z.; Huang, Y.-Q. Partial melting of lithospheric mantle and formation of the early cretaceous alkaline rocks in the Guandimiao ree deposit, Luxi Terrane, Eastern China. *Minerals* **2022**, *12*, 670. [CrossRef]
74. Williams-Jones, A.E.; Vasyukova, O.V. Niobium, critical metal, and progeny of the mantle. *Econ. Geol.* **2023**, *118*, 837–856. [CrossRef]
75. Yong, T.; Linnen, R.L.; McNeil, A.G. An experimental study of pyrochlore solubility in peralkaline granitic melts. *Econ. Geol.* **2023**, *118*, 209–223. [CrossRef]
76. Han, W.S.; Ran, M.J.; Lua, X.; Jiang, C.L.; Chen, W. The effects of multielement basicity on niobium-bearing phase reconstruction in low grade niobium rougher concentrate. *Miner. Eng.* **2024**, *217*, 108951. [CrossRef]
77. Zurevinski, S.E.; Mitchell, R.H. Extreme compositional variation of pyrochlore-group minerals at the oka carbonatite complex, quebec: Evidence of magma mixing? *Can. Mineral.* **2004**, *42*, 1159–1168. [CrossRef]
78. Yaroshevskii, A.A.; Bagdasarov, Y.A. Geochemical diversity of minerals of the pyrochlore group. *Geochem. Int.* **2009**, *46*, 1245–1266. [CrossRef]
79. Han, W.; Ran, M.; Lu, X.; Jiang, C.; Zhou, Y.; Chen, W. Effects of oxygen on the phase reconstruction of low-grade complicated niobium resources during cooling process. *JOM* **2025**, *77*, 6443–6453. [CrossRef]
80. Wu, B.; Hu, Y.-Q.; Bonnetti, C.; Xu, C.; Wang, R.-C.; Zhang, Z.-S.; Li, Z.-Y.; Yin, R. Hydrothermal alteration of pyrochlore group minerals from the Miaoya carbonatite complex, central China and its implications for Nb mineralization. *Ore Geol. Rev.* **2021**, *132*, 104059. [CrossRef]
81. Han, W.; Ran, M.; Lu, X.; Chen, W. Study on the transformation and growth behavior of niobium-bearing phase in slag during cooling process. In Proceedings of the Asia Steel 2024 Conference, Changsha, China, 4–7 September 2024.
82. Fan, H.-R.; Yang, K.-F.; Hu, F.-F.; Liu, S.; Wang, K.-Y. The giant Bayan Obo REE-Nb-Fe deposit, China: Controversy and ore genesis. *Geosci. Front.* **2016**, *7*, 335–344. [CrossRef]
83. Liu, S.; Ding, L.; Fan, H.-R.; Yang, K.-F.; Tang, Y.-W.; She, H.-D.; Hao, M.-Z. Hydrothermal genesis of Nb mineralization in the giant Bayan Obo REE-Nb-Fe deposit (China): Implicated by petrography and geochemistry of Nb-bearing minerals. *Precambrian Res.* **2020**, *348*, 105864. [CrossRef]
84. Ren, Y.; Yang, X.; Yang, X.; Ling, M.; Liu, Y. Mineralogical study on the distribution regularity of niobium in various types of ores in the giant Bayan Obo Fe-REE-Nb deposit. *Ore Geol. Rev.* **2023**, *161*, 105602. [CrossRef]
85. Ren, Y.; Yang, X.; Wang, X. Occurrence of niobium in biotite-type Fe-REE-Nb ore in the Bayan Obo deposit. *Solid Earth Sci.* **2023**, *8*, 25–28. [CrossRef]

86. Yang, K.-F.; Fan, H.-R.; Santosh, M.; Hu, F.-F.; Wang, K.-Y. Mesoproterozoic carbonatitic magmatism in the Bayan Obo deposit, Inner Mongolia, North China: Constraints for the mechanism of super accumulation of rare earth elements. *Ore Geol. Rev.* **2011**, *40*, 122–131. [CrossRef]
87. Congzhong, T.; Wenjie, Z.; Fengyang, L.; Yuxin, L.; Zhijun, Z.; Zhengyao, L. A comprehensive review on recent progress in beneficiation of Nb-bearing minerals /Nb ores. *Miner. Eng.* **2024**, *212*, 108710. [CrossRef]
88. Liu, C.J.; Qiu, J.Y.; Liu, Z.Y. Phase equilibria in the system CaO-SiO_2-La_2O_3-Nb_2O_5 at 1400 °C. *Metals* **2021**, *11*, 1892. [CrossRef]
89. Liu, C.; Qiu, J.; Liu, Z.; Zhu, D.; Wang, Y.; Jiang, M. Adjacent relations of primary phase fields and invariant reactions of the system CaO-SiO_2-Nb_2O_5-La_2O_3. *J. Am. Ceram. Soc.* **2021**, *104*, 2398–2409. [CrossRef]
90. Qiu, J.Y.; Liu, C.J.; Liu, Z.Y.; Zheu, D.Y. Isothermal phase diagram of CaO-SiO_2-Nb_2O_5-La_2O_3 system at 1300 °C, 1200 °C. *Ceram. Int.* **2020**, *46*, 4832–4842. [CrossRef]
91. Qiu, J.Y.; Liu, C.J.; Liu, Z.Y.; Zhu, D.Y. Liquidus phase diagram of CaO-SiO_2-La_2O_3-Nb_2O_5 system with w(La_2O_3) = 15 to 25 Pct. *Metall. Mater. Trans. B-Process Metall. Mater. Process. Sci.* **2020**, *51*, 1190–1200. [CrossRef]
92. Qiu, J.Y.; Liu, C.J.; Liu, Z.Y.; Yu, Z. Phase equilibria in low basicity region of CaO-SiO_2-Nb_2O_5-(5 wt%, 10 wt%, 15 wt%) La_2O_3 system. *J. Rare Earths* **2020**, *38*, 100–107. [CrossRef]
93. Sun, L.; Liu, Z.; Jiang, M. Phase equilibria of CaO-SiO_2-La_2O_3-Nb_2O_5 system in reducing atmosphere. *Metals* **2022**, *12*, 768. [CrossRef]
94. Liu, C.J.; Qiu, J.Y.; Liu, Z.Y.; Zhu, D.Y.; Wang, Y.G. Phase equilibria in the system CaO-SiO_2-Nb_2O_5-La_2O_3 at 1473 K with pO_2=$10^{-15.47}$ atm. *Ceram. Int.* **2020**, *46*, 7711–7718. [CrossRef]
95. Liu, Z.Y.; Sun, L.F.; Zhao, H.; Xiang, T.Y.; Qiu, J.Y.; Jiang, M.F. Isothermal phase diagram of CaO-SiO_2-Nb_2O_5-5wt% Fe_2O_3-TiO_2 system at 1200 °C. *Ceram. Int.* **2022**, *48*, 31636–31651. [CrossRef]
96. Liu, Z.; Sun, L.; Pan, X.; Jiang, M. Isothermal phase diagram of CaO-SiO_2-Nb_2O_5-5wt% Fe_2O_3-TiO_2 system at 1100 °C. *J. Phase Equilibria Diffus.* **2024**, *45*, 849–862. [CrossRef]
97. Zhang, B.; Ma, C.; Wang, R.; Liu, C.; Jiang, M. Selective smelting reduction of metal oxides in REE-Nb-Fe deposit. *JOM* **2022**, *74*, 993–1001. [CrossRef]
98. Zhang, B.; Liu, J.; Jia, X.; Xing, T.; Liu, C.; Jiang, M. Mineral phase reconstruction of Bayan Obo tailings by smelting reduction and crystallization control of molten slag containing niobium, rare earth and titanium. *Miner. Eng.* **2024**, *214*, 108780. [CrossRef]
99. Jia, X.-L.; Zhang, B.; Cui, L.; Liu, C.-J.; Jiang, M.-F. Separation and enrichment of valuable elements from slag containing rare earth, niobium and titanium via Fe–Si bath smelting reduction. *J. Iron Steel Res. Int.* **2024**, *32*, 1990–2000. [CrossRef]
100. Beyer, C.; Berndt, J.; Tappe, S.; Klemme, S. Trace element partitioning between perovskite and kimberlite to carbonatite melt: New experimental constraints. *Chem. Geol.* **2013**, *353*, 132–139. [CrossRef]
101. Han, W.; Ran, M.; Lu, X.; Chen, W. Growth behaviors of calciobetafite during phase reconstruction process of Bayan Obo niobium rougher concentrate. *J. Cent. South Univ. (Sci. Technol.)* **2025**, *56*, 468–477.
102. Roy, J.J.; Rarotra, S.; Krikstolaityte, V.; Zhuoran, K.W.; Cindy, Y.D.I.; Tan, X.Y.; Carboni, M.; Meyer, D.; Yan, Q.Y.; Srinivasan, M. Green recycling methods to treat lithium-ion batteries e-waste: A circular approach to sustainability. *Adv. Mater.* **2022**, *34*, 2103346. [CrossRef]
103. Rautela, R.; Yadav, B.R.; Kumar, S. A review on technologies for recovery of metals from waste lithium-ion batteries. *J. Power Sources* **2023**, *580*, 233428. [CrossRef]
104. Liu, C.; Lin, J.; Cao, H.; Zhang, Y.; Sun, Z. Recycling of spent lithium-ion batteries in view of lithium recovery: A critical review. *J. Clean. Prod.* **2019**, *228*, 801–813. [CrossRef]
105. Schirmer, T.; Qiu, H.; Goldmann, D.; Stallmeister, C.; Friedrich, B. Influence of P and Ti on phase formation at solidification of synthetic slag containing Li, Zr, La, and Ta. *Minerals* **2022**, *12*, 310. [CrossRef]
106. Hampel, S.; Alhafez, I.A.; Schirmer, T.; Merkert, N.; Wunderlich, S.; Schnickmann, A.; Li, H.; Fischlschweiger, M.; Fittschen, U.E.A. Engineering compounds for the recovery of critical elements from slags: Melt characteristics of Li_5AlO_4, $LiAlO_2$, and $LiAl_5O_8$. *ACS Omega* **2024**, *9*, 24584–24592. [CrossRef]
107. Strube, F.; Guy, B.M.; Pereira, L.; Ebert, D.; Zgheib, A.; Fischer, M.; Möckel, R.; Schmidt, A.; Rudolph, M. Batch flotation of lithium-bearing slag—A special focus on the phase properties of engineered artificial minerals for enhancing the recycling of end-of-life lithium-ion batteries. *Minerals* **2025**, *15*, 334. [CrossRef]
108. Abreu, D.A.d.; Schnickmann, A.; Chakrabarty, S.; Fischlschweiger, M.J.; Schirmer, T.; Fabrichnaya, O. Stability of crystalline compounds in slag systems mainly composed of Li_2O-SiO_2-CaO-MnOx. *JOM* **2024**, *76*, 6472–6486. [CrossRef]
109. Acker, S.; Namyslo, J.C.; Rudolph, M.; Strube, F.; Fittschen, U.E.A.; Qiu, H.; Goldmann, D.; Schmidt, A. Polyether-tethered imidazole-2-thiones, imidazole-2-selenones and imidazolium salts as collectors for the flotation of lithium aluminate and spodumene. *RSC Adv.* **2023**, *13*, 6593–6605. [CrossRef]
110. Zakeri, A.; Tafaghodi, L. A review of the current progress in high-temperature recycling strategies for recovery of rare-earth elements from magnet waste. *J. Sustain. Metall.* **2025**, *11*, 88–113. [CrossRef]

111. Gao, J.T.; Xue, K.R.; Lan, X.; Guo, Z.C. Phase equilibrium relationship of CaO-SiO_2-La_2O_3 system and crystallization behaviors of RE phases. *JOM* **2023**, *75*, 3521–3531. [CrossRef]
112. Gao, J.T.; Xu, H.H.; Lan, X.; Guo, Z.C. Phase equilibrium of the CaO-SiO_2-Al_2O_3-Ce_2O_3 system: A basis for recovering REEs from RE-Containing slag. *Ceram. Int.* **2022**, *48*, 34907–34914. [CrossRef]
113. Li, M.C.; Li, R.S.; Zhang, T.S. Phase equilibria of SiO_2-Ce_2O_3-CaO-25 wt% Al_2O_3 system at 1673 K-1773 K. *Ceram. Int.* **2022**, *48*, 31614–31626. [CrossRef]
114. Lan, X.; Gao, J.T.; Li, Y.; Guo, Z.C. Thermodynamics and kinetics of REEs in CaO-SiO_2-CaF_2-Ce_2O_3 system: A theoretical basis toward sustainable utilization of REEs in REE-Bearing slag. *Ceram. Int.* **2021**, *47*, 6130–6138. [CrossRef]
115. Shi, J.J.; Zhai, Y.M.; Qiu, Y.C.; Jiang, C.L.; Hou, C.L.; Dong, J.J.; Li, J.Z. Phase equilibria of the CaO-SiO_2-CeO_2-Al_2O_3-MgOsystem at 1300 °C, 1400 °C. *JOM* **2024**, *76*, 4598–4607. [CrossRef]
116. Ma, Z.; Zhao, Z.W.; Guo, W.T.; Guo, X.Q. Effect of TiO_2 addition cooling rate on crystallization behavior of separated slag containing low-grade, R.E. *ISIJ Int.* **2023**, *63*, 1274–1280. [CrossRef]
117. Ma, Z.; Zhao, Z.W.; Guo, X.Q.; Guo, W.T. Selective precipitation and non-isothermal crystallization kinetics of britholite from low grade REE-bearing slag. *J. Rare Earths* **2023**, *41*, 1812–1818. [CrossRef]
118. Zhao, F.H.; Deng, Y.C.; Xin, W.B.; Zhang, J.; Jiang, Y.J.; Cao, Z.J.; Wang, L.Y. Investigation of the effect of P_2O_5 and CaF_2 on the crystallization behavior of La_2O_3-bearing calcium-silicate-aluminum slags using the single hot thermocouple technique. *Metall. Res. Technol.* **2024**, *121*, 503. [CrossRef]
119. Guo, W.T.; Shi, K.H.; Liu, X.K.; Sun, Z.L.; Liu, X.J. Effects of phosphorus structures on the crystallization behavior of rare earth phase in CaO-SiO_2-CaF_2-La_2O_3 Slag. *Trans. Indian Inst. Met.* **2024**, *77*, 697–705. [CrossRef]
120. Lan, X.; Gao, J.T.; Xue, K.R.; Guo, Z.C. Selective separation and crystal characterization of RE-phases from RE-bearing slag systems: Calcium cerite and cefluosil. *J. Am. Ceram. Soc.* **2023**, *106*, 2130–2138. [CrossRef]
121. Lan, X.; Gao, J.T.; Xu, H.H.; Guo, Z.C. In situ separation and characterization of britholite crystals in RE-bearing slag via supergravity. *J. Am. Ceram. Soc.* **2022**, *105*, 5966–5974. [CrossRef]
122. Lan, X.; Gao, J.T.; Xue, K.R.; Xu, H.H.; Guo, Z.C. A new finding and technology for selective separation of different REEs from CaO-SiO_2-CaF_2-P_2O_5-Fe_3O_4-RE_2O_3 system. *Sep. Purif. Technol.* **2022**, *293*, 121121. [CrossRef]
123. Zhang, S.; Zheng, K.; Jiang, J.; Zhang, S.; Xu, G. Effect of operating parameters on high-temperature selective enrichment and precipitation of titanium component in Ti-bearing blast furnace slag and the precipitation mechanism of perovskite. *J. Mater. Res. Technol.* **2021**, *15*, 2686–2696. [CrossRef]
124. Zhang, L.; Zhang, L.N.; Wang, M.Y.; Li, G.Q.; Sui, Z.T. Precipitation selectivity of perovskite phase from Ti-bearing blast furnace slag under dynamic oxidation conditions. *J. Non-Cryst. Solids* **2007**, *353*, 2214–2220. [CrossRef]
125. Zhang, L.; Zhang, L.N.; Wang, M.Y.; Li, G.Q.; Sui, Z.T. Recovery of titanium compounds from molten Ti-bearing blast furnace slag under the dynamic oxidation condition. *Miner. Eng.* **2007**, *20*, 684–693. [CrossRef]
126. Wang, Z.; Sun, H.-Y.; Zhu, Q.-S. Effects of the continuous cooling process conditions on the crystallization and liberation characteristics of anosovite in Ti-bearing titanomagnetite smelting slag. *Int. J. Miner. Metall. Mater.* **2019**, *26*, 1120–1128. [CrossRef]
127. Ma, G.C.; Tian, J.K.; Shen, Y.Y. Structure and magnetic properties of (Ni,Fe)Fe_2O_4 derived from nickel slag via molten oxidation. *Mater. Today Commun.* **2024**, *40*, 109537. [CrossRef]
128. Li, B.; Du, X.Y.; Shen, Y.Y.; Zhang, Z.L.; Rong, T.L. Nonisothermal crystallization, growth, and shape control of magnetite crystals in molten nickel slag during continuous cooling. *Metall. Mater. Trans. B-Process Metall. Mater. Process. Sci.* **2022**, *53*, 1816–1826. [CrossRef]
129. Shen, Y.Y.; Chong, J.K.; Huang, Z.N.; Tian, J.K.; Zhang, W.J.; Tang, X.C.; Ding, W.W.; Du, X.Y. Thermodynamics and kinetics of FeO transferred to Fe_3O_4 in modified nickel slag during molten oxidation process. *Mater. Res. Express* **2019**, *6*, 096551. [CrossRef]
130. Shen, Y.Y.; Huang, Z.N.; Zhang, Y.Y.; Zhong, J.K.; Zhang, W.J.; Yang, Y.; Chen, M.; Du, X.Y. Transfer behavior of Fe element in nickel slag during molten oxidation and magnetic separation processes. *Mater. Trans.* **2018**, *59*, 1659–1664. [CrossRef]
131. Yan, Z.H.; Zhao, Q.; Han, C.Z.; Mei, X.H.; Liu, C.J.; Jiang, M.F. Effects of iron oxide on crystallization behavior and spatial distribution of spinel in stainless steel slag. *Int. J. Miner. Metall. Mater.* **2024**, *31*, 292–300. [CrossRef]
132. Huo, X.T.; Zhang, X.; Ding, Z.H.; Zhang, M.; Guo, M. A clean approach for detoxification of industrial chromium-bearing stainless steel slag: Selective crystallization control and binary basicity effect. *J. Hazard. Mater.* **2023**, *446*, 130746. [CrossRef] [PubMed]
133. Wang, Y.-J.; Zhang, X.-P.; Zhang, J.-B.; Peng, L.-J.; Li, J.-G. Optimizing vanadium converter slag utilization: Targeted enrichment and stabilization of vanadium through non-equilibrium solidification. *Mater. Tehnol.* **2024**, *58*, 339–348. [CrossRef]